

Interplay of charge and spin coherence in Landau-Zener-Stückelberg-Majorana interferometry

Hugo Ribeiro,^{1,*} J. R. Petta,^{2,3} and Guido Burkard¹

¹*Department of Physics, University of Konstanz, D-78457 Konstanz, Germany*

²*Department of Physics, Princeton University, Princeton, New Jersey 08544, USA*

³*Princeton Institute for the Science and Technology of Materials (PRISM), Princeton University, Princeton, New Jersey 08544, USA*

(Received 6 October 2012; published 26 June 2013)

We study Landau-Zener dynamics in a double quantum dot filled with two electrons, where the spin states can become correlated with charge states and the level velocity can be tuned in a time-dependent fashion. We show that a correct interpretation of experimental data is only possible when finite-time effects are taken into account. In addition, our formalism allows the study of partial adiabatic dynamics in the presence of phonon-mediated hyperfine relaxation and charge-noise-induced dephasing. Our findings demonstrate that charge noise severely impacts the visibility of Landau-Zener-Stückelberg-Majorana interference fringes. This indicates that charge coherence must be treated on an equal footing with spin coherence.

DOI: [10.1103/PhysRevB.87.235318](https://doi.org/10.1103/PhysRevB.87.235318)

PACS number(s): 03.67.Lx, 71.70.Jp, 73.21.La, 73.23.Hk

I. INTRODUCTION

Electron spins trapped in quantum dots (QDs) are promising candidates for implementing a scalable quantum computer.^{1,2} Most of the DiVincenzo criteria, which state physical requirements a system must fulfill to achieve quantum computing, have been achieved with spin qubits, including initialization,³ readout,⁴ and coherent control.^{5–7} While experimental progress has been impressive, many of these methods are not yet accurate enough to allow large-scale quantum computing with single spins. A key challenge can be appreciated by considering the relevant time scales associated with the spin dynamics. In GaAs quantum dot devices, it is well known that the hyperfine interaction leads to a randomly fluctuating nuclear field $B_n \sim 2$ mT, which results in a 10–20 ns inhomogeneous spin dephasing time.^{5,8,9} For comparison, the Rabi period obtained in a GaAs double quantum dot (DQD) using conventional electron spin resonance (ESR) is on the order of 110 ns.⁶ The use of spin-orbit-driven electric dipole spin resonance (EDSR) in GaAs leads to even slower Rabi periods of roughly 210 ns.⁷ Therefore, in the case of single-spin rotations, gate operation times are nearly an order of magnitude slower than the inhomogeneous spin dephasing time. This issue is not specific to GaAs-based nanostructures. In InAs nanowires, where the spin-orbit interaction is larger than in GaAs, a Rabi period of ~ 17 ns (Ref. 10) was reported. However, it still is twice as long as the spin dephasing time of ~ 8 ns.

Viewed from a different perspective, the maximum ac field generated in DQD ESR experiments is on the order of 2 mT, which is the same magnitude as the fluctuating nuclear field.⁶ As a result, single-spin rotations in GaAs qubits follow imperfect trajectories on the Bloch sphere, resulting in a reduced oscillation visibility and gate errors.⁶ Single-spin selectivity imposes an additional challenge upon the development of a spin-based quantum processor. Magnetic fields generated in ESR are difficult to localize on the nanometer scale. Without g -factor control, or local magnetic field gradients, the spins located in a quantum register would rotate at the same rate in the presence of a global ESR field. The long-term goal is to be

able to drive selective single-spin rotations, without affecting neighboring spins that are on average only 20–50 nm away.

Instead of using the spin-up and -down states of a single electron, the qubit basis states can be represented by two (out of four) two-electron spin states confined in a DQD.¹¹ For a qubit whose basis states are encoded in the singlet S and triplet T_0 spin states of a DQD, the two-electron exchange interaction allows for fast single-qubit gates (hundreds of picoseconds).⁵ Recent experiments^{12,13} have also demonstrated the possibility of realizing a conditional two-qubit gate. Within this two-spin version of a qubit, the two-qubit gate realized in Ref. 5 can be interpreted as a single-qubit operation. However, the exchange interaction only allows for rotations about a single axis, whereas to generate arbitrary rotations one needs two perpendicular rotation axes. The generation of a nuclear magnetic field gradient¹⁴ provides rotations about a second, noncollinear axis. While remarkable, this method also presents some difficulties when it has to be extended to a large number of qubits. It requires that the nuclear polarization is controlled in each DQD to create the desired gradient field. An advantage of this method is that the generation of the nuclear field gradient reduces nuclear spin fluctuations, resulting in an increase in the spin dephasing time.¹⁵

Recently, it has been proposed to use a two-spin basis consisting of the singlet S and triplet T_+ spin states.^{16–18} Quantum control of the S - T_+ qubit relies on Landau-Zener-Stückelberg-Majorana^{19–22} (LZSM) physics, which occurs in the system when the S - T_+ qubit is repeatedly swept through the hyperfine mediated S - T_+ anticrossing. This all-electrical method also has the advantage of addressing individually each quantum dot.

LZSM physics describing the passage of a two-level quantum system through an anticrossing can be applied to different fields of physics and chemistry.²³ In quantum information science, LZSM theory describes accurately the observed interference fringes (Stückelberg oscillations) of a superconducting qubit driven back and forth through its anticrossing.²⁴ The LZSM description also accurately describes the coherent manipulation of a two-spin qubit

encoded in the S and triplet T_+ spin states, with dynamics driven by repeated passages through a hyperfine-mediated anticrossing.^{16,17} In self-assembled quantum dots, LZSM theory has been used to design high-fidelity all-optical control of spin-based qubits.^{25–27}

In this paper, we develop a quantum master equation to describe partial adiabatic passages between the spin singlet S and triplet T_+ states in the presence of both the fluctuating Overhauser field and the fluctuating charge environment. With our theory, we show charge dynamics can significantly hinder LZSM interferometry of spin states. While most of the interesting spin dynamics happens in the (1,1) charge configuration, with one electron per dot, initialization and measurements are done deep in the (2,0) charge configuration, where both electrons are in the left dot. Here, (l,r) denotes the number of electrons in the left and right dots. Crossing the $(1,1) \leftrightarrow (2,0)$ interdot charge transition necessarily involves charge dynamics. Since superpositions of charge states dephase on shorter time scales than superpositions of spin states, it is essential to consider this fast effective decoherence mechanism when spin and charge degrees of freedom become correlated during spin-qubit evolution.^{28,29} In particular, we use our formalism to analyze spin-charge dynamics associated with detuning pulses that have a tunable level velocity, with a high-level velocity away from the anticrossing and a slow-level velocity in the vicinity of the anticrossing.¹⁸

The paper is organized as follows. We start by reviewing standard Landau-Zener theory, which is valid for an infinitely long ramp through an anticrossing with a constant level velocity. In Sec. II, we review the solution of the finite-time LZSM model, which can be used to model realistic experiments, and we demonstrate within the scope of this theory how fine tuning of the level velocity can be used to increase the visibility of the quantum oscillations. Section III focuses on the physical implementation of LZSM physics in a two-electron spin qubit. We derive an effective Hamiltonian describing the dynamics of the states in the vicinity of the S- T_+ anticrossing. Compared to previously derived effective Hamiltonians,¹⁷ we include the effects of charge superposition states in the spin-dependent anticrossing. The last part of the section is devoted to the derivation of a master equation that describes the evolution of the density matrix. In Sec. IV, we first compare solutions of the master equation obtained with experimental pulse profiles and measurements performed on a GaAs double quantum dot. We then show theory results for the singlet return probability for which we explore the effects of charge-induced decoherence.

II. ADIABATIC CONTROL OF A QUANTUM TWO-LEVEL SYSTEM

There are numerous problems in physics that deal with the physics of two-level systems. The most common example is Rabi's formula,³⁰ which describes the occupation of a two-level system that is driven by a coherent field. In quantum information science, Rabi oscillations are widely used, e.g., to manipulate an electron spin confined in a QD.³¹ Another widely studied problem involving only two quantum levels is adiabatic passage, which is commonly employed in nuclear magnetic resonance.³² The physics of adiabatic passage can

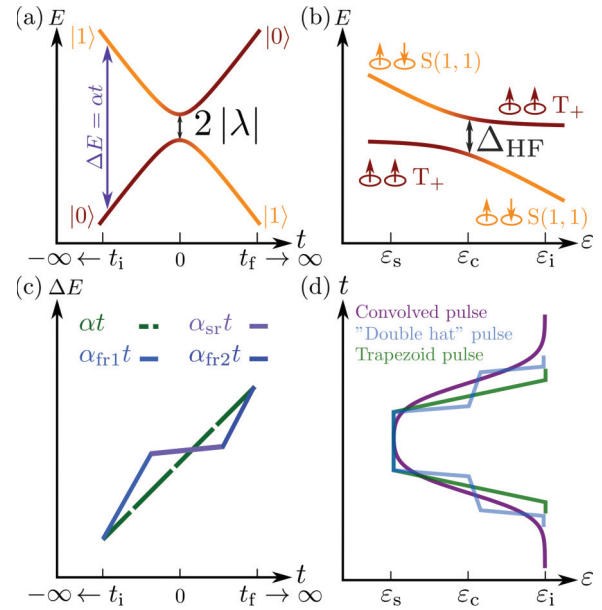


FIG. 1. (Color online) (a) The Landau-Zener-Stückelberg-Majorana (LZSM) problem. The LZSM model addresses the problem of a two-level system that is swept through an anticrossing. It assumes an infinitely long ramp (i.e., propagation from $t_i \rightarrow -\infty$ to $t_f \rightarrow \infty$), a constant coupling constant λ leading to a splitting $2|\lambda|$ at $t = 0$, and an energy difference between the levels that varies linearly with time $\Delta E(t) = \alpha t$. Its main result gives the nonadiabatic transition probability P_{LZSM} . An extension of the model to finite times resolves the problem of infinite energies and undefined phases. (b) Singlet and triplet T_+ energies in a QD as a function of detuning ε , where $\varepsilon_i = \varepsilon(t_i)$ and $\varepsilon_s = \varepsilon(t_f)$. The two-electron QD is a physical realization of the LZSM model. Here, the hyperfine coupling of the two spin states leads to a splitting Δ_{HF} . (c) The LZSM model assumes a constant level velocity α . In order to increase adiabaticity, one can lower α , but in order to keep short pulses it is preferable to use multi rise-time pulses. (d) Comparison of possible pulses that can be used to manipulate the S- T_+ qubit. In terms of total propagation time, “double-hat” pulses are a good compromise between conventional trapezoid and convolved pulses.

be found in a variety of systems, and several theoretical models have been developed to describe different kinds of adiabatic processes.^{33–42} There is, however, a particular description that has proven to be applicable in many distinct fields of physics: the Landau-Zener^{19,20} model. We refer to it in this paper as the LZSM model since it was independently studied by Stückelberg²¹ and Majorana.²²

The Hamiltonian studied in the LZSM model describes a system with two energy levels [see Fig. 1(a)] that are coupled by an off-diagonal matrix element λ , $H(t) = -(\alpha t/2)\sigma_z + \lambda\sigma_x$, where σ_z and σ_x are Pauli matrices, and $\alpha = d(E_2(t) - E_1(t))/dt$. The main result of the theory is the asymptotic expression for the nonadiabatic transition probability when the propagation lasts from $t_i = -\infty$ to $t_f = \infty$:

$$P_{\text{LZSM}} = e^{-\frac{2\pi\lambda^2}{\alpha\hbar}}. \quad (1)$$

Here, we use a generalization of the LZSM model, known as the finite-time LZSM model.⁴³ It resolves the problem of

the energy divergence when $t_{f,i} = \pm\infty$, and in contrast to the simple case it yields the relative phase between the states, which is crucial for predicting the coherent time evolution of any quantum system. Particularly, knowledge of the relative phase is essential in LZSM interferometry^{21,23} in which the system is driven back and forth across an anticrossing. The driving generates quantum interference between states, which is directly observable in the nonadiabatic (or adiabatic) transition probability.

A. Finite-time Landau-Zener-Stückelberg-Majorana propagator

The unitary evolution operator defined by the LZSM Hamiltonian¹⁹⁻²²

$$H(t) = \begin{pmatrix} -\frac{\alpha}{2}t & \lambda \\ \lambda & \frac{\alpha}{2}t \end{pmatrix} \quad (2)$$

is given by⁴³

$$U(t_f, t_i) = \begin{pmatrix} u_{11}(t_f, t_i) & u_{12}(t_f, t_i) \\ u_{21}(t_f, t_i) & u_{22}(t_f, t_i) \end{pmatrix}, \quad (3)$$

where 1 (2) refers to the states $|0\rangle$ ($|1\rangle$) with

$$\begin{aligned} u_{11}(t_f, t_i) &= u_{22}^*(t_f, t_i) \\ &= \frac{\Gamma(1 - i\eta^2)}{\sqrt{2\pi}} [D_{i\eta^2}(e^{-\frac{i\pi}{4}} \tau_f) D_{i\eta^2-1}(e^{\frac{3i\pi}{4}} \tau_i) \\ &\quad + D_{i\eta^2}(e^{\frac{3i\pi}{4}} \tau_f) D_{i\eta^2-1}(e^{-\frac{i\pi}{4}} \tau_i)] \end{aligned} \quad (4)$$

and

$$\begin{aligned} u_{12}(t_f, t_i) &= -u_{21}^*(t_f, t_i) \\ &= \frac{\Gamma(1 - i\eta^2)}{\sqrt{2\pi}\eta} e^{\frac{i\pi}{4}} [-D_{i\eta^2}(e^{-\frac{i\pi}{4}} \tau_f) D_{i\eta^2}(e^{\frac{3i\pi}{4}} \tau_i) \\ &\quad + D_{i\eta^2}(e^{\frac{3i\pi}{4}} \tau_f) D_{i\eta^2}(e^{-\frac{i\pi}{4}} \tau_i)]. \end{aligned} \quad (5)$$

Here, $\tau = \sqrt{\alpha/\hbar}t$ is a dimensionless time, $\eta = \lambda/\sqrt{\alpha\hbar}$ is a dimensionless coupling, $\Gamma(z)$ is the gamma function,⁴⁴ and $D_\nu(z)$ is the parabolic cylinder function.⁴⁵ By definition, $t = 0$ is set at the anticrossing. The usual LZSM formula (1) is retrieved from the modulus square of Eq. (4) when taking the limit $t_i \rightarrow -\infty$ and $t_f \rightarrow \infty$.

The LZSM propagator fully determines the partial adiabatic dynamics of a quantum two-level system. In the case where the two-level system encodes a qubit, Eq. (3) allows the design of single-qubit operations. This method has been used to control superconducting qubits^{23,24} and more recently to implement a qubit encoded in the spin of a two-electron state.^{16,17} However, since the spin states are weakly coupled, $\eta < 1$, it is hard to achieve an equally weighted coherent superposition of spin states and fully explore the entire qubit state space. In order to achieve full control over the spin qubit, it would be necessary to perform slower sweeps, i.e., to increase η by making α smaller. However, the LZSM equation requires an exponential increase in the propagation time in order to achieve a fully adiabatic transition. In a real physical system, this method is unpractical because the pulse duration needs to remain shorter than the coherence time of the two-level system.

B. Observing finite-time effects

As demonstrated in Ref. 18, it is possible to use more complex pulses to increase the balance of the populations while keeping the manipulation time below the decoherence times. The key idea relies on an observation based on the finite-time LZSM model. For a slow-level velocity α , which favors adiabatic passage, most of the population change occurs in the vicinity of the anticrossing. It is therefore possible to use detuning pulses that have a time-dependent level velocity. Let us consider two types of pulses, as illustrated in Figs. 1(c) and 1(d). The first is a conventional linear pulse, which is standard in LZSM theory. The second pulse profile consists of linear detuning ramps in a fast-slow-fast rise-time sequence, which we refer to as “double-hat” pulse. The unitary evolution of such a general sequence can be written using Eq. (3) as

$$\begin{aligned} U(t_f, t_i) &= U_{\text{fast2}}(t_f, t_2) U_{\text{slow}}(t_2, t_1) U_{\text{fast1}}(t_1, t_i) \\ &= \begin{pmatrix} \tilde{u}_{11}(t_f, t_i) & \tilde{u}_{12}(t_f, t_i) \\ \tilde{u}_{21}(t_f, t_i) & \tilde{u}_{22}(t_f, t_i) \end{pmatrix}. \end{aligned} \quad (6)$$

Here, $t_1 = t_i + t_{\text{fr1}}$, $t_2 = t_i + t_{\text{fr1}} + t_{\text{sr}}$, and $t_f = t_i + t_{\text{fr1}} + t_{\text{sr}} + t_{\text{fr2}}$, where $t_{\text{fr}j}$ is the propagation time associated to the j th fast sequence, and t_{sr} corresponds to the slow sequence. We use this notation to refer to the corresponding level velocities α_j , dimensionless times τ_j , and dimensionless couplings η_j .

In addition to the already mentioned and studied advantages “double-hat” pulses offer, they also provide sensitive means to explore finite-time effects. These are in general neglected when describing experiments because the more convenient LZSM scattering approach²³ has been sufficient to reproduce experimental results.^{16,24} However, to implement high-fidelity quantum gates, it will be necessary to accurately describe the dynamics of the qubit and thus take into account finite-time propagation.

In Fig. 2, we compare adiabatic transition probabilities obtained with double-hat pulses and conventional trapezoid pulses (cf. inset of Fig. 2). Here, an adiabatic transition refers to a transition where the system remains in an instantaneous energy eigenstate. The details of the leading edge (the trailing edge is identical but reversed) of the double-hat pulse are $t_{\text{fr1}} = t_{\text{fr2}} = 0.1$ ns, the starting position of the slow-level velocity ramp is defined by the condition $\Delta E_i - \Delta E_{i,\text{sr}} = -2 \mu\text{eV}$, where ΔE_i is the initial energy difference between the uncoupled eigenstates and $\Delta E_{i,\text{sr}}$ the energy difference at the beginning of the slow part of the pulse. We choose $\alpha_{\text{sr}} = 500 \text{ eVs}^{-1}$ and $\lambda = 70 \text{ neV}$. We impose the same total propagation time on the linear pulse as for the double hat, from which we obtain the level velocity α_{si} for the linear pulse

$$\alpha_{\text{si}} = \frac{\Delta E_f - \Delta E_i}{t_{\text{fr1}} + t_{\text{fr2}} + t_{\text{sr}}}. \quad (7)$$

The adiabatic transition probability P_a is plotted as a function of ΔE_f . Here, ΔE_f indicates the energy difference between the states when the pulse has reached its maximal amplitude. Different values of ΔE_f are obtained by adding an offset to ΔE_i , while keeping the length of pulse (thus α_{si} and the different α_j of the double hat) constant. Since we are interested in finite-time effects, we impose $\Delta E_f < 0$ for trapezoid pulses, which reflects that the system is not detuned through the anticrossing. This condition is relaxed for double-hat pulses,

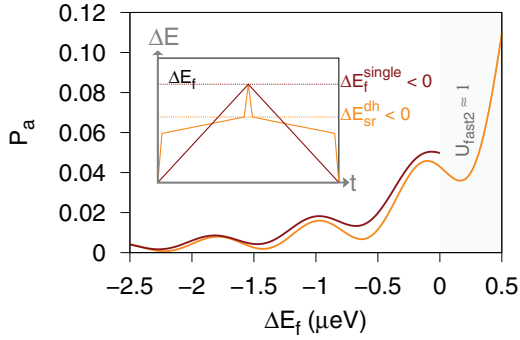


FIG. 2. (Color online) Comparison of the adiabatic transition probability P_a for a double hat (orange) and a linear pulse (red) with $t_w = 0$ as a function of ΔE_f . (Inset) Pulse profiles used to obtain P_a . The maximal offset for the single rise-time pulse is chosen such that the system is never driven through the anticrossing ($\Delta E_f^{\text{single}} < 0$). The maximal offset for double-hat pulses is determined by the condition that the system cannot be driven through the anticrossing ($\Delta E_{sr}^{\text{dh}} < 0$). For double-hat pulses, the values of P_a between $0 < \Delta E_f < 0.5 \mu\text{eV}$ originate from the slow portion of the pulse, which brings the system close to the anticrossing. In this range, the magnitude of P_a is not due to the second fast rise-time portion of the pulse, which drives the system through the anticrossing.

for which we impose $\Delta E_f < 0.5 \mu\text{eV}$. This is equivalent, with our choice of parameters, to letting the system be driven up to the anticrossing with the slow component of the double hat. This condition can be written as $\Delta E_{sr}^{\text{dh}} < 0$, i.e., the energy difference at the end of the slow rise-time component is smaller than 0.

Our results show for the trapezoid pulse what is expected from a finite-time LZSM theory.⁴³ There is a small probability for an adiabatic transition if the system is detuned to close proximity of the anticrossing. If one compares this result with values of P_a obtained with the double hat, it seems that there is no enhancement. Moreover, one would have a tendency to associate values of P_a between $0 < \Delta E_f < 0.5 \mu\text{eV}$ as originating from the second fast-rise portion of the pulse, which drives the system through the anticrossing. However, for the particular double hat we are considering here, we have $U_{\text{fast2}} \approx 1$. This means that the values of P_a in the range $0 < \Delta E_f < 0.5 \mu\text{eV}$ are due to the system being brought close to the anticrossing with the slow portion of the pulse, for which $\eta \gtrsim 1$. This is in contrast with trapezoid pulses, or any single rise-time pulse, for which $\Delta E_f > 0$ implies that most of the magnitude of P_a comes from the system being driven through the anticrossing.

To illustrate our last statement, in Fig. 3 we present a comparison between P_a obtained with a double-hat pulse as described previously and a “truncated double hat,” which is missing the second fast detuning ramp (cf. inset Fig. 3). To compare P_a between the two pulses, we choose the x axis to describe ΔE_f at the end of the slow detuning pulse. We shift the values obtained with a double hat along the x axis by an amount $\Delta E_{\text{fast2}} = 0.5 \mu\text{eV}$ to compare between the two different pulses. We clearly see that for both cases, P_a is nearly identical.

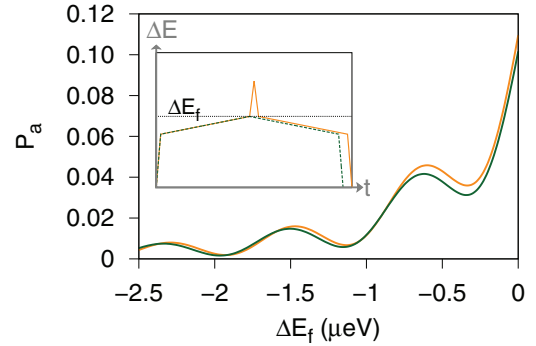


FIG. 3. (Color online) Comparison of the adiabatic transition probability P_a for a double hat (orange) and a truncated double hat (green), which is missing the second fast rise-time component, as a function of ΔE_f at the end of the slow detuning pulse. (Inset) Pulse profiles used to obtain P_a . The results obtained with a double hat are shifted by an amount ΔE_{fast2} on the x axis to allow for comparison. We conclude from these results that the state of the system is hardly changed during the second fast detuning pulse.

III. ADIABATIC CONTROL OF A S-T₊ QUBIT

In the following, we apply the previously developed ideas to a physical implementation of a LZSM driven qubit. We focus on the two-spin S-T₊ implementation in a GaAs DQD (Refs. 16 and 17) [see Fig. 1(b)]. Although the dynamics of the system under double-hat pulses has already been studied experimentally,¹⁸ there is still a need to gain a better understanding of the charge-noise-induced spin dephasing. We will show, among other things, that the measurement of finite-time LZSM oscillations can provide a tool to qualitatively access the strength of charge noise.

A. Double quantum dot spin states

The spin-preserving part of the Hamiltonian describing the confinement of electrons in a DQD in the presence of an external magnetic field can be written using a simple two-site hopping model

$$H_0 = \sum_{\substack{i=1,2 \\ \sigma=\uparrow,\downarrow}} \left(\varepsilon_i + \frac{1}{2} g^* \mu_B B \sigma \right) c_{i\sigma}^\dagger c_{i\sigma} + u \sum_i c_{i\uparrow}^\dagger c_{i\uparrow} c_{i\downarrow}^\dagger c_{i\downarrow} + \tau \sum_{\sigma} (c_{1\sigma}^\dagger c_{2\sigma} + \text{H.c.}). \quad (8)$$

The index $i = 1, 2$ labels the dot number and $\sigma = \uparrow, \downarrow = \pm 1$ the spin of the electron. We denote the energy of a single confined electron by ε_i and the Zeeman energy associated with its spin is given by $g^* \mu_B B \sigma / 2$, where g^* denotes the effective Landé g factor, μ_B the Bohr magneton, B the strength of the external magnetic field. The operators $c_{i\sigma}$ and $c_{i\sigma}^\dagger$ describe, respectively, the annihilation and creation of an electron in dot i with spin σ . Two electrons occupying the same QD give rise to an intradot Coulomb energy u . The last term of Eq. (8) accounts for electron tunneling between the dots with strength τ . We neglect the interdot Coulomb interaction because it only produces a constant shift of the energy levels.

Since most recent experiments on a DQD system are operated in a regime with at most two electrons, we can project

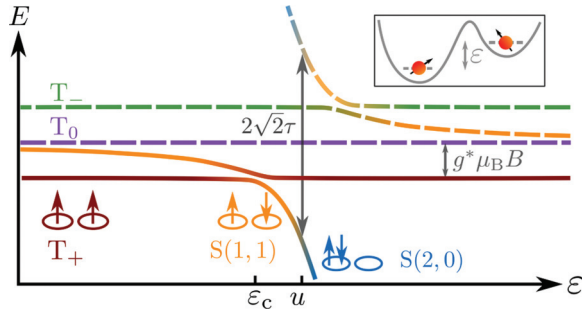


FIG. 4. (Color online) Energy diagram for the relevant states in the DQD as a function of ε . The spin states for the implementation of the qubit are the hybridized singlet S and the triplet T_+ .

Eq. (8) into the subspace spanned by the charge configurations $(0,2)$, $(2,0)$, and $(1,1)$.^{5,14,16,46,47} The diagonalization of the resulting Hamiltonian leads to six low-energy states which are superpositions of the singlets $S(0,2)$, $S(2,0)$, and $S(1,1)$ as well as the triplets $T_0(1,1)$, $T_+(1,1)$, and $T_-(1,1)$. The triplet states with two particles in the same dot must have electrons occupying higher-energy orbitals due to the Pauli principle. This results in a relatively high separation in energy ($\sim 400 \mu\text{eV}$) from a singlet with both electrons occupying the same dot.⁴⁸ Consequently, the triplet states with two electrons in the same dot can be safely neglected for the purpose of the current study.

An energy-level diagram is shown in Fig. 4, where we plot the energies of the relevant two-electron spin states as a function of detuning $\varepsilon = \varepsilon_1 - \varepsilon_2$. The degeneracy of the singlets $S(1,1)$ and $S(2,0)$ at $\varepsilon = u$, as well as between $S(1,1)$ and $S(0,2)$ at $\varepsilon = -u$, is lifted due to tunneling, which results in a splitting of the levels by $2\sqrt{2}\tau$. The degeneracy between the spin singlet S and spin triplet T_0 is lifted due to the exchange interaction.⁴⁹ This property has allowed the encoding of a spin qubit in these two spin states and its manipulation via the exchange interaction.⁵

Here, we concentrate on a particular value of detuning that we have denoted by ε_c in the energy-level diagram. This point corresponds to the crossing of the singlet state with the triplet T_+ state and is special because there is an anticrossing due to the hyperfine interaction between the electron spins and nuclear spins of the host material. It has been demonstrated experimentally¹⁶ and theoretically¹⁷ that coherent control of the S- T_+ qubit can be achieved by detuning the system from an initially prepared $S(2,0)$ through the hyperfine-mediated anticrossing.

The hyperfine interaction is described by the effective Hamiltonian

$$H_{\text{HF}} = \mathbf{S}_1 \cdot \mathbf{h}_1 + \mathbf{S}_2 \cdot \mathbf{h}_2 \quad (9)$$

between the electron spin \mathbf{S}_i and the effective magnetic fields \mathbf{h}_i that are generated by the nuclear spins \mathbf{I}_i in dot i . The Overhauser field operators $\mathbf{h}_i = \sum_{k=1}^{n_i} A_i^k \mathbf{I}_i^k$ describe the nuclear spin bath. Here, n_i is the number of nuclei in dot i and $A_i^k = v_{ik} v_0 |\psi_i(\mathbf{r}_k)|^2$ is the hyperfine coupling constant with the k th nucleus in dot i , with $\psi_i(\mathbf{r}_k)$ the electron wave function, v_0 the volume of the unit cell, and v_{ik} the hyperfine coupling strength. A more convenient form of the hyperfine interaction is obtained by introducing the spin ladder operators

$S_i^\pm = S_i^x \pm iS_i^y$ and $h_i^\pm = h_i^x \pm ih_i^y$, which yield

$$H_{\text{HF}} = \frac{1}{2} \sum_i (2S_i^z h_i^z + S_i^+ h_i^- + S_i^- h_i^+). \quad (10)$$

The longitudinal part of H_{HF} is diagonal and its contribution will add to the energy of the triplet state. The transverse part

$$H_{\text{HF}}^\perp = \frac{1}{2} \sum_i (S_i^+ h_i^- + S_i^- h_i^+) \quad (11)$$

generates the so-called flip-flop process that results in an energy gap at ε_c and allows for mixing of the S and T_+ spin states.^{8,9,15}

B. S- T_+ effective Hamiltonian

In this section, we derive an effective 2×2 Hamiltonian that describes the dynamics of the S- T_+ spin states near the hyperfine-induced anticrossing. Before doing so, we start by making a few considerations based on LZSM theory to determine which states play a negligible role in the dynamics. Since Eq. (8) describes a series of anticrossings, it is possible to use the results of Refs. 50 and 51 where a formula for the nonadiabatic transition probability of a multiple crossings LZSM model has been derived. It was shown that for well-separated anticrossings,⁵¹ we have $P_k = \prod_{j=1}^k \exp(-2\pi\lambda_j^2/\hbar\alpha_j)$, where P_k is the nonadiabatic transition probability after the k th anticrossing. This formula is a product of k LZSM probabilities, which reflects the independence between the set of anticrossings.

This model can directly be applied to the DQD system for magnetic fields on the order of a few hundreds of mT, where the charge anticrossing and both of the hyperfine-induced anticrossings (T_+ and T_-) are well separated. Here, we demonstrate that if the system is initialized in the singlet $S(2,0)$, then the detuning pulses allowing for mixing of the lowest-energy hybridized singlet state and triplet T_+ cannot populate the higher-energy hybridized singlet state and consequently the triplet T_- . Let us consider that the hyperfine coupling strength is on the order of a hundred nanoelectron volts $\lambda_{\text{HF}} = 100 \text{ neV}$. This value is consistent with experimental findings. In Ref. 16, a strength of 60 neV has been reported. For our choice of λ_{HF} , we find $P_{\text{LZSM}} = 0.5$ for $\alpha \simeq 138 \text{ eVs}^{-1}$. This would correspond to an equally weighted superposition of the qubit states. However, this is only true if there is no population transfer to the higher hybridized singlet level as predicted by the equation for P_k . By evaluating the population transfer between $S(2,0)$ and $S(1,1)$ with the LZSM formula for $\alpha = 138 \text{ eVs}^{-1}$ and $\lambda_{\text{charge}} = \sqrt{2}\tau \simeq 7.1 \mu\text{eV}$, we find $P_{\text{LZSM}} \simeq 0$, within the numerical precision of our calculation, which indicates that there is no population transfer.

From the previous considerations, we have shown that it is safe to neglect the higher-energy hybridized singlet state as well as the triplet T_- , but the importance of T_0 remains to be determined. Here, we rely on recent experimental results⁴⁷ which demonstrate that only a certain type of detuning pulses lead to mixing between T_+ , T_0 , and the ground-state singlet. Moreover, as the results of Ref. 47 indicate, it is possible to identify in interference patterns the presence of T_0 in the dynamics.⁵²

Finally, we conclude that it is possible to restrict the Hilbert space to two states: $T_+(1,1)$ and the lowest-energy hybridized singlet S . In order to derive an analytical expression for the latter, we start by considering the projection of Eq. (8) onto the states $T_+(1,1)$, $S(1,1)$, and $S(2,0)$. We find

$$H_0(\varepsilon) = \begin{pmatrix} g^* \mu_B B & 0 & 0 \\ 0 & 0 & \sqrt{2}\tau \\ 0 & \sqrt{2}\tau & u - \varepsilon \end{pmatrix}. \quad (12)$$

The diagonalization of Eq. (12) yields two hybridized singlets and the triplet state T_+ :

$$|S\rangle = c(\varepsilon)|S(1,1)\rangle + \sqrt{1 - c(\varepsilon)^2}|S(2,0)\rangle, \quad (13)$$

$$|S'\rangle = c'(\varepsilon)|S(1,1)\rangle + \sqrt{1 - c'(\varepsilon)^2}|S(2,0)\rangle, \quad (14)$$

$$|T\rangle = |T_+(1,1)\rangle, \quad (15)$$

with respective energies

$$E_S(\varepsilon) = \frac{1}{2}[u - \varepsilon - \sqrt{8\tau^2 + (u - \varepsilon)^2}], \quad (16)$$

$$E_{S'}(\varepsilon) = \frac{1}{2}[u - \varepsilon + \sqrt{8\tau^2 + (u - \varepsilon)^2}], \quad (17)$$

$$E_T = g^* \mu_B B. \quad (18)$$

The charge admixture coefficients $c(\varepsilon)$ and $c'(\varepsilon)$ are

$$c(\varepsilon) = \frac{\varepsilon - u - \sqrt{8\tau^2 + (u - \varepsilon)^2}}{\sqrt{8\tau^2 + [-\varepsilon + u + \sqrt{8\tau^2 + (\varepsilon - u)^2}]^2}}, \quad (19)$$

$$c'(\varepsilon) = \frac{\varepsilon - u + \sqrt{8\tau^2 + (u - \varepsilon)^2}}{\sqrt{8\tau^2 + [\varepsilon - u + \sqrt{8\tau^2 + (\varepsilon - u)^2}]^2}}. \quad (20)$$

We can now make the following basis change:

$$T(\varepsilon) = \begin{pmatrix} 1 & 0 & 0 \\ 0 & c(\varepsilon) & c'(\varepsilon) \\ 0 & \sqrt{1 - c^2(\varepsilon)} & \sqrt{1 - c'^2(\varepsilon)} \end{pmatrix}, \quad (21)$$

such that

$$H_0^{\text{diag}}(\varepsilon) = T(\varepsilon)^\dagger H_0(\varepsilon) T(\varepsilon) = \begin{pmatrix} g^* \mu_B B & 0 & 0 \\ 0 & E_S & 0 \\ 0 & 0 & E_{S'} \end{pmatrix}. \quad (22)$$

We add now to the Hamiltonian defined in Eq. (12) the hyperfine interaction defined in Eq. (9). Since we are not interested in describing the nuclear spin dynamics, but its effect on the two-spin states S and T_+ , we can model the action of the Overhauser field operators by introducing a classical stochastic variable which accounts for fluctuations in the nuclear spin ensemble.^{8,9,15} By setting

$$\mathbf{h}_i = g^* \mu_B \mathbf{B}_{n,i}, \quad (23)$$

we can interpret $\mathbf{B}_{n,i}$ as the effective random magnetic field acting on S_i . Under normal experimental conditions we have $k_B T \gg g_n \mu_n B$, where g_n and μ_n are the nuclear g factor and magneton. The nuclear spins can, in this limit, be assumed to be completely unpolarized, resulting in a Gaussian distribution

of nuclear fields^{8,9,15}

$$p(B_{n,i}) = \frac{1}{\sqrt{2\pi}\sigma} e^{-\frac{B_{n,i}^2}{2\sigma^2}}, \quad (24)$$

with $\delta = A/g^* \mu_B \sqrt{n}$, the hyperfine coupling constant $A \approx 90 \mu\text{eV}$, and the approximate number of nuclei overlapping with the electronic wave function $n \approx 10^5 - 10^6$. By defining $B_{n,i}^\pm = B_{n,i}^x \pm iB_{n,i}^y$, the hyperfine Hamiltonian can be written by analogy with Eq. (10) as

$$H_{\text{HF}} = \frac{1}{2} \sum_i (2S_i^z B_{n,i}^z + S_i^+ B_{n,i}^- + S_i^- B_{n,i}^+). \quad (25)$$

The longitudinal part of H_{HF} can be included in the energy of the triplet state $g^* \mu_B B \rightarrow g^* \mu_B (B + B_{n,1}^z + B_{n,2}^z)$, while the transverse part

$$H_{\text{HF}}^\perp = \frac{1}{2} \sum_i (S_i^+ B_{n,i}^- + S_i^- B_{n,i}^+) \quad (26)$$

mixes the spin states $|S\rangle$ and $|T\rangle$. We therefore find that the full Hamiltonian, in the $\{|T_+(1,1)\rangle, |S(1,1)\rangle, |S(2,0)\rangle\}$ basis, describing the dynamics of the singlet S and triplet T_+ near the hyperfine anticrossing, is given by

$$H_{S-T_+}(\varepsilon) = \begin{pmatrix} g^* \mu_B \tilde{B} & \lambda & 0 \\ \lambda & 0 & \sqrt{2}\tau \\ 0 & \sqrt{2}\tau & (u - \varepsilon) \end{pmatrix}, \quad (27)$$

where $\tilde{B} = B + B_{n,1}^z + B_{n,2}^z$ and

$$\lambda = \langle S(1,1) | H_{\text{HF}}^\perp | T_+(1,1) \rangle = g^* \mu_B (B_{n,2}^- - B_{n,1}^-) / 2\sqrt{2}. \quad (28)$$

In the basis that diagonalizes Eq. (12), the Hamiltonian defined in Eq. (27) reads as

$$\tilde{H}_{S-T_+}(\varepsilon) = \begin{pmatrix} g^* \mu_B \tilde{B} & c(\varepsilon)\lambda & c'(\varepsilon)\lambda \\ c(\varepsilon)\lambda & E_S(\varepsilon) & 0 \\ c'(\varepsilon)\lambda & 0 & E_{S'}(\varepsilon) \end{pmatrix}. \quad (29)$$

The projection of Eq. (29) onto the Hilbert space spanned by $\{|S\rangle, |T\rangle\}$ leads to the effective 2×2 Hamiltonian describing the dynamics at the singlet-triplet T_+ anticrossing. Taking into account that the detuning is time dependent $\varepsilon = \varepsilon(t)$, we finally obtain

$$H(t) = E_S[\varepsilon(t)]|S\rangle\langle S| + \tilde{E}_T|T\rangle\langle T| + f[\varepsilon(t)](|S\rangle\langle T| + \text{H.c.}), \quad (30)$$

where E_S is defined in Eq. (16) and $\tilde{E}_T = g^* \mu_B \tilde{B}$. This effective Hamiltonian differs from previous derivations^{17,53} in the coupling $f(t) = c[\varepsilon(t)]\lambda$, which is time dependent. Here, $c[\varepsilon(t)]$ and λ are given in Eqs. (19) and (28). As it can be seen from the functional form of $f(t)$, the effective coupling strength between the spin states depends on the charge state (Fig. 5). This result is rather natural since the matrix element between S and T_+ goes to zero when the detuning is such that $S = S(2,0)$ and $T_+ = T_+(1,1)$, i.e., $\langle S | H_{\text{HF}}^\perp | T_+ \rangle \rightarrow 0$ for $\varepsilon \gg u$. It also implies that the physics described by Eq. (30) goes beyond standard LZSM theory with a constant coupling. However, since both Hamiltonians describe adiabatic passage through an anticrossing, we can assume that the dynamics is qualitatively similar. We can therefore expect that our previous

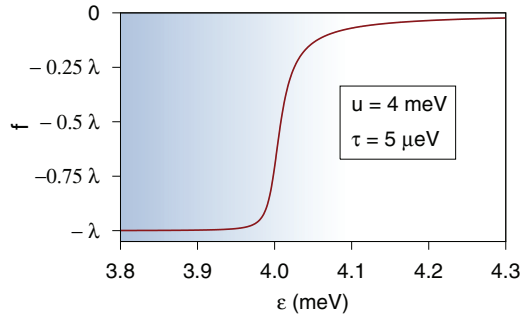


FIG. 5. (Color online) The effective hyperfine-mediated coupling between $|S\rangle$ and $|T\rangle$ is a function of detuning. This is a consequence of the state $|S\rangle$ being a superposition of different charge states.

discussion about enhancement of adiabaticity based on LZSM physics remains valid. Furthermore, due to the peculiar form of $f(t)$ (cf. Fig. 5), we can assume that it is possible to observe finite-time interferometry phenomena in close vicinity of the anticrossing.

C. Master equation

In order to compare our theory with experimental measurements, it is not sufficient to solve the Hamiltonian dynamics provided by Eq. (30) because some important phenomena that can influence the outcome of the experiment are not taken into account. Among these are spin relaxation due to phonon-

assisted hyperfine interaction⁵⁴ and charge fluctuations that lead to dephasing of the qubit states.⁵⁵ These phenomena can be taken into account in a quantum master-equation formalism for the density matrix. In the Lindblad formalism,^{56,57} the time evolution can be expressed as

$$\dot{\rho} = -\frac{i}{\hbar} [H, \rho] + \frac{1}{2} \sum_{j=1}^{N^2-1} ([L_j \rho, L_j^\dagger] + [L_j, \rho L_j^\dagger]). \quad (31)$$

The operators L_j are called Lindblad operators^{56,57} and they describe the dissipative effect of the environment on the system in the Born-Markov approximation, which consists of two assumptions that lead to Eq. (31). The Born approximation supposes a weak coupling between the system and the bath, while the Markov approximation neglects any type of bath memory effects during the system evolution. To fully describe the effect of the environment, one needs $N^2 - 1$ operators where N is the dimension of the system's Hilbert space.^{56,57} For the case of a two-level system, the Lindblad operators are $L_1 = \sqrt{\Gamma_-} \sigma_-$, $L_2 = \sqrt{\Gamma_+} \sigma_+$, and $L_3 = \sqrt{\Gamma_\varphi} \sigma_z$, where σ_- and σ_+ are spin ladder operators and σ_z is the z Pauli matrix. They respectively describe relaxation from the excited state to the ground state with rate Γ_- , relaxation from the ground state to the excited state with rate Γ_+ , and pure dephasing with rate Γ_φ .

By substituting Eq. (30) into (31) and using the expression of the Lindblad operators, the first-order differential equation for the S- T_+ density matrix can be written as

$$\begin{pmatrix} \dot{\rho}_{11} \\ \dot{\rho}_{12} \\ \dot{\rho}_{21} \\ \dot{\rho}_{22} \end{pmatrix} = \begin{pmatrix} -\Gamma_+ & \frac{i}{\hbar} f(t) & -\frac{i}{\hbar} f(t) & \Gamma_- \\ \frac{i}{\hbar} f(t) & -\frac{i}{\hbar} [E_S(t) - \tilde{E}_T] - \frac{1}{2}(\Gamma_+ + \Gamma_- + 4\Gamma_\varphi) & 0 & -\frac{i}{\hbar} f(t) \\ -\frac{i}{\hbar} f(t) & 0 & \frac{i}{\hbar} [E_S(t) - \tilde{E}_T] - \frac{1}{2}(\Gamma_+ + \Gamma_- + 4\Gamma_\varphi) & \frac{i}{\hbar} f(t) \\ \Gamma_+ & -\frac{i}{\hbar} f(t) & \frac{i}{\hbar} f(t) & -\Gamma_- \end{pmatrix} \times \begin{pmatrix} \rho_{11} \\ \rho_{12} \\ \rho_{21} \\ \rho_{22} \end{pmatrix}. \quad (32)$$

This system of four coupled ordinary differential complex equations can be reduced to a system of three coupled ordinary differential equations (Bloch equations) by introducing new real variables defined by

$$x = \rho_{12} + \rho_{21}, \quad y = i(\rho_{12} - \rho_{21}), \quad z = \rho_{11} - \rho_{22}. \quad (33)$$

This set of variables is completed by the conservation of probability condition

$$\rho_{11} + \rho_{22} = 1. \quad (34)$$

Substituting Eqs. (33) and (34) into (32), one finds the system of ordinary differential equations for the new variables

$$\dot{x} = -\frac{E_S - \tilde{E}_T}{\hbar} y - \frac{1}{2}(\Gamma_+ + \Gamma_-)x - 2\Gamma_\varphi x, \quad (35)$$

$$\dot{y} = \frac{E_S - \tilde{E}_T}{\hbar} x - 2\frac{f}{\hbar} z - \frac{1}{2}(\Gamma_+ + \Gamma_-)y - 2\Gamma_\varphi y, \quad (36)$$

$$\dot{z} = 2\frac{f}{\hbar} y - (\Gamma_+ + \Gamma_-)z + \Gamma_- - \Gamma_+. \quad (37)$$

Here, we assume that relaxation occurs through phonon-assisted hyperfine interaction. Since we are dealing with small energy transfers, we consider only piezophonons.⁵⁸ The Hamiltonian describing the coupling between the logical qubit states [i.e., the instantaneous energy eigenstates of Eq. (30)] and the phonons is given by $H_{\text{qp}} = \sigma_z \otimes U_{\text{ph}}$, with

$$U_{\text{ph}}(\mathbf{r}, t) = \sum_{\nu, \mathbf{q}} \sqrt{\frac{\hbar}{2\rho\omega_{\nu, \mathbf{q}}}} A_{\nu, \mathbf{q}} [e^{i(\mathbf{q} \cdot \mathbf{r} - \omega_{\nu, \mathbf{q}} t)} b_{\nu, \mathbf{q}}^\dagger + \text{H.c.}], \quad (38)$$

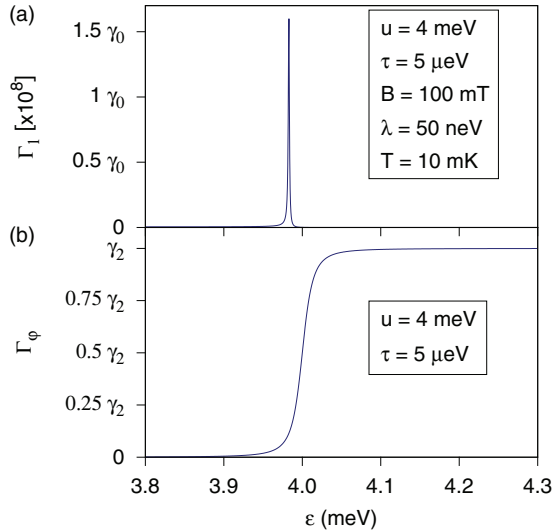


FIG. 6. (Color online) (a) Relaxation rate $\Gamma_1(\varepsilon)$ obtained for $B = 100$ mT. Here, we consider hyperfine-mediated flip-flops of the electron spin accompanied by emission or absorption of phonons. The relaxation rate is maximal for $\varepsilon = \varepsilon_c$ where $|E_S^d(\varepsilon) - E_T^d| \ll k_B T$. This results in a strong mixing of the spin states due to thermal fluctuations. (b) Charge-noise-induced dephasing rate $\Gamma_2(\varepsilon)$. The dephasing rate is assumed to have a functional dependence proportional to $1 - c(\varepsilon)^2$ to ensure that dephasing related to charge noise is weaker when the system is in a (1,1) charge configuration.

and σ_z is the pseudospin z -Pauli matrix for $|S\rangle$ and $|T\rangle$. Here, $b_{v,q}^\dagger$ ($b_{v,q}$) creates (annihilates) a phonon with polarization v and wave vector q . $A_{v,q}$ is the effective piezoelectric modulus, which depends only on the direction of q .

The rates Γ_+ and Γ_- can be derived using Redfield theory.^{59,60} We have

$$\Gamma_{\pm} = 4 |\langle 0 | \sigma_z | 1 \rangle|^2 J_{\pm}(\omega), \quad (39)$$

where $|0\rangle$ and $|1\rangle$ are the qubit states [i.e., in our case the eigenstates of Eq. (30)], ω the angular frequency defined by the difference in energy of the qubit states, and the spectral densities $J_{\pm}(\omega)$ are defined by

$$J_{\pm}(\omega) = \int_0^{\infty} dt e^{\mp i\omega t} \langle U_{\text{ph}}(\mathbf{r}, 0) U_{\text{ph}}(\mathbf{r}, t) \rangle. \quad (40)$$

Here, $\langle \dots \rangle = \text{Tr}[\dots \rho_{\text{ph}}]$ with ρ_{ph} the density matrix of the phonon bath at thermal equilibrium.

The evaluation of Eq. (40) leads to

$$J_+(\omega) = \sum_v \frac{3\langle A^2 \rangle}{4\pi^2 \rho c_v^3 \hbar} \omega n(\omega) \quad (41)$$

and

$$J_-(\omega) = \sum_v \frac{3\langle A^2 \rangle}{4\pi^2 \rho c_v^3 \hbar} \omega [1 + n(\omega)], \quad (42)$$

with c_v the sound velocity and $n(\omega)$ the Bose-Einstein occupation number $n(\omega) = [\exp(\beta \hbar \omega) - 1]^{-1}$, where $\beta = 1/k_B T$. k_B is the Boltzmann's constant and T is the phonon bath temperature, and $\langle A^2 \rangle$ denotes an average piezoelectric modulus. In the following, we denote the result of the sum over v by γ_0 .

Since Γ_+ and Γ_- can be related to each other by considering the limiting case of thermal equilibrium, Eqs. (37) can be simplified to include only two independent rates. If the system reaches thermal equilibrium then the detailed balance equation $\rho_{11}^{\text{th}} \Gamma_+ = \rho_{22}^{\text{th}} \Gamma_-$ holds. Moreover, the populations are given by the canonical ensemble $\rho_{ii}^{\text{th}} = \exp(-\beta E_i)/Z$, with Z the partition function. This yields

$$\frac{\Gamma_+}{\Gamma_-} = \frac{\rho_{22}^{\text{th}}}{\rho_{11}^{\text{th}}} = e^{-\beta \hbar \omega}, \quad (43)$$

where we used $\hbar \omega = \sqrt{[E_S(\varepsilon) - \tilde{E}_T]^2 + 4f^2(\varepsilon)}$, which is the energy difference between the eigenstates of Eq. (30).

Combining the results of Eqs. (39) and (41)–(43), we find that

$$\Gamma_1(\varepsilon) = \Gamma_+ + \Gamma_- = \gamma_0 \frac{f^2(\varepsilon)}{\hbar^2 \omega} \coth\left(\frac{\hbar \omega}{2k_B T}\right). \quad (44)$$

This function is plotted against ε in Fig. 6(a), and has a peak at $\varepsilon = \varepsilon_c$ where $\hbar \omega \ll k_B T$ resulting in a strong mixing of the states due to thermal fluctuations.

Pure dephasing can originate from orbital effects. In our current description of the problem, we have neglected that the wave functions of the singlet $|S(2,0)\rangle$ and triplet $|T_+(1,1)\rangle$ couple differently to the background charge environment due to their different charge configurations. Thus, a superposition state of the form $|\psi\rangle = \alpha|S(2,0)\rangle + \beta|T_+(1,1)\rangle$ is sensitive to background charge fluctuations (charge noise), which leads to dephasing of the state $|\psi\rangle$.^{8,55} If the qubit is in a superposition with the same charge state $|\varphi\rangle = \alpha|S(1,1)\rangle + \beta|T_+(1,1)\rangle$, then the effects of charge noise are assumed to become weaker. Therefore, we choose to write the charge-induced dephasing as

$$\Gamma_{\varphi}(\varepsilon) = \gamma_2 [1 - |c(\varepsilon)|^2], \quad (45)$$

where γ_2 is the charge noise rate. In Fig. 6, we plot the rates $\Gamma_1(\varepsilon)$ and $\Gamma_{\varphi}(\varepsilon)$.

Finally, the Bloch equations, written in a matrix form, and describing the dynamics around the S- T_+ anticrossing, are

$$\hbar \begin{pmatrix} \dot{x} \\ \dot{y} \\ \dot{z} \end{pmatrix} = \begin{pmatrix} -\frac{1}{2}\hbar\{\Gamma_1[\varepsilon(t)] + 4\Gamma_{\varphi}[\varepsilon(t)]\} & -E_S[\varepsilon(t)] + \tilde{E}_T & 0 \\ E_S[\varepsilon(t)] - \tilde{E}_T & -\frac{1}{2}\hbar\{\Gamma_1[\varepsilon(t)] + 2\Gamma_{\varphi}[\varepsilon(t)]\} & -2\lambda c[\varepsilon(t)] \\ 0 & 2\lambda c[\varepsilon(t)] & -\hbar\Gamma_1[\varepsilon(t)] \end{pmatrix} \begin{pmatrix} x \\ y \\ z \end{pmatrix} \pm \hbar \begin{pmatrix} 0 \\ 0 \\ \gamma_1 \end{pmatrix}. \quad (46)$$

The different signs in front of the inhomogeneous term come from the fact that the states $|S\rangle$ and $|T\rangle$ exchange their roles as ground and excited states of the system at $\varepsilon = \varepsilon_c$. The spontaneous relaxation rate γ_1 is given by

$$\gamma_1 = \gamma_0 \frac{f^2(\varepsilon)}{\hbar^2 \omega}. \quad (47)$$

IV. RESULTS

In the following, we first present a comparison between experimental and theory results obtained with experimental pulse profiles, which were measured at the output port of the waveform generator, and experimentally determined $E_S(\varepsilon)$ and $c(\varepsilon)$. We then show further theory results for which we study the effect of charge dynamics and phonon-mediated hyperfine relaxation. For this purpose, we have solved Eq. (46) for different γ_0 's and γ_2 's.

The singlet return probability is obtained by solving Eq. (46) for different realizations of λ . The average value of P_S is then calculated according to

$$P_S = \frac{1}{N} \sum_{i=1}^N \frac{1}{2} (1 + z^{(i)}), \quad (48)$$

where $z^{(i)}$ is the i th solution of $z(t)$ in Eq. (46).

A. Experimental observation of finite-time effects

We consider a double-hat detuning pulse whose profile is shown in the inset of Fig. 7(a). The leading edge has a rise time of 0.1 ns and an amplitude A_{1f} , which is followed by a slow ramp with rise time t_{slow} and amplitude $A_s = -0.065$ meV. A 0.1 ns rise-time pulse shifts the detuning to its maximal value of -0.39 meV, where the detuning is held constant for a time interval t_w . The trailing edge of the pulse is simply the reverse of the leading edge. The conversion between gate voltage and energy is performed using the measured lever arm ~ 0.13 meV/mV.^{29,61} In Fig. 7, we compare experiment and theory for $t_{slow} = 4$ ns, $A_{1f} = -0.26$ meV.

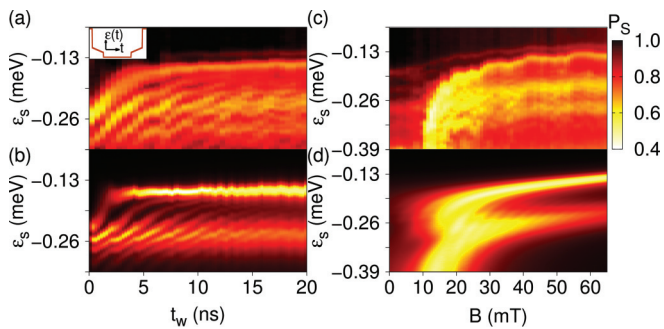


FIG. 7. (Color online) (a) Measurements of P_S as a function of t_w and ε_s for $A_{1f} = -0.26$ meV, $t_{slow} = 4$ ns, and $B = 55$ mT. Double-hat pulses allow the observation of nonadiabatic transitions when the system is driven slowly to close proximity of the anticrossing. (b) Theoretical predictions obtained using a pulse profile obtained at the output of the waveform generator and parameters from (a). (c) P_S plotted as a function of B and ε_s for $t_w = 20$ ns reveals the spin funnel. Parameters are $A_{1f} = -0.26$ meV and $t_{slow} = 4$ ns. (d) Theoretical calculations for the same parameters as in (c).

P_S is plotted as a function of t_w and ε_s for $B = 55$ mT in Figs. 7(a) and 7(b). A “spin funnel” that is obtained using the spectroscopy method developed in Ref. 5 with a waiting time $t_w = 20$ ns is shown in Fig. 7(c) along with the corresponding theory plot in Fig. 7(d). Since the experimental cycles have a short period of $5 \mu s$, there is a buildup of nuclear polarization that generates a gradient field.¹⁴ To take this into account in our model, we add a mean to the nuclear field distributions (24). It is sufficient to consider only a mean ξ_1^x for $B_{n,1}^x$ because only the magnitude of the gradient field plays a role in the dynamics. This can be easily understood by considering a rotation about the z axis of the coordinate system that brings the x axis to coincide with the direction of $\mathbf{B}_{n,2}^\perp - \mathbf{B}_{n,1}^\perp$. Parameters used in the theory panels are $\delta = 1$ mT, $\xi_1^x = 10$ mT, $\gamma_0 = 10^{-2}$, and $\gamma_2 = 10^8$ s $^{-1}$.

Both the experimental results and numerical simulations show enhanced interference visibility within the region between $\varepsilon_s \sim -0.19$ meV and ~ -0.29 meV. This region should correspond to values of P_S determined by the slow rise-time component of the pulse, as demonstrated in Ref. 18. The position of the anticrossing is located at ~ -0.14 meV from the data shown in Figs. 7(a) and 7(c). Moreover, since $A_{1f} = -0.26$ meV, $A_s = -0.065$ meV, and the maximal pulse amplitude is -0.39 meV, the high-contrast region should be located between -0.21 and -0.27 meV, in good agreement with our results.

As discussed in Sec. II B, the visibility of the oscillation pattern contained between $\varepsilon_s \sim -0.14$ meV and ~ -0.21 meV cannot result from the second fast rise-time portion of the pulse. Although it drives the system through the anticrossing, the level velocity is too high to allow for large-magnitude nonadiabatic transition probabilities. Thus, as we showed in Figs. 2 and 3 by considering a finite-time LZSM model, we are able to observe a nonadiabatic transition event due to a slow-level velocity pulse that brings the system to close vicinity of the anticrossing, but without driving it through.

To ensure that we are observing finite-time effects, we consider a second double-hat pulse that has a different A_{1f} , which changes the relative starting and stopping position of the slow rise-time component of the pulse. As a consequence,

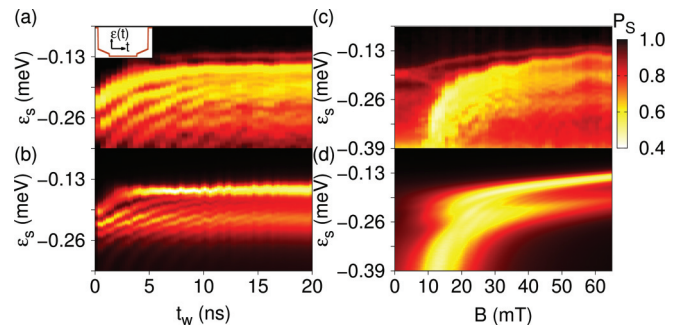


FIG. 8. (Color online) Experimentally [(a) and (c)] and theoretically [(b) and (d)] obtained LZSM interference patterns and spin funnels. Here, $A_{1f} = -0.29$ meV, $t_{slow} = 4$ ns, and $B = 55$ mT. The waiting time for the spin funnel is $t_w = 20$ ns. The interference patterns differ from results presented in Fig. 7, indicating that the evolution of the system is not only sensitive to the level velocity, but also the time at which the change in level velocity happens.

the relative propagation times t_i and t_f , which are defined by setting $t = 0$ at the anticrossing, are also modified.

We consider a second pulse with $A_{1f} = -0.29$ meV, for which the results are presented in Fig. 8. First, we observe that the high-contrast region is shifted towards more positive detunings, as expected. Second, we notice the overall difference between the interference pattern in Figs. 7 and 8, panels (a) and (b). This dissimilarity can only be explained by different phase accumulation due to distinct t_i and t_f . In the usual scattering description of LZSM interferometry, the transition probability only depends on the level velocity at the anticrossing and on the coupling strength. But here, these two quantities have remained unchanged. These results show the importance of using finite-time models to describe adiabatic passage experiments.

We also anticipate, for LZSM driven qubits, the possibility to manipulate the states by keeping a constant driving and instead change the relative starting and stopping positions of the detuning pulse.

B. Effects of phonon-mediated hyperfine relaxation and charge-induced dephasing

In this section, we consider a detuning pulse $\varepsilon(t)$ with an amplitude of $\varepsilon_s - \varepsilon_i = 0.2$ meV. The pulse reaches an amplitude of 0.12 meV in 0.1 ns, it is then slowed down until it reaches an amplitude of 0.1325 meV, and finally it is brought to its maximal amplitude in 0.1 ns. The rise time t_{slow} of the slow part of the pulse can be tuned freely. Here, we compute P_S for $t_{\text{slow}} = 8$ ns. In Figs. 9(a)–9(d), we present the singlet return probability as a function of ε_s and waiting time t_w for $B = 100$ mT, $u = 4$ meV, $\tau = 5$ μeV , and different values of γ_0 and γ_2 . The interference fringes are characterized, for $\varepsilon_s < \varepsilon_c$, by three distinct regions showing an alternate oscillation amplitude for P_S . The darker regions coincide with detunings for which the passage through the anticrossing happened during one of the fast rise times of $\varepsilon(t)$. Similarly, the bright region between $\varepsilon_s \simeq 3.900$ –3.915 meV coincides with a passage through the anticrossing with the slow rise-time portion of the detuning pulse. Experimentally measured interference patterns exhibit identical behavior.

Our results also clearly show coherent evolution of the qubit for $\varepsilon_s > \varepsilon_c$ [Fig. 9(e), blue and purple trace, $\gamma_2 = 10^8$ s $^{-1}$]. This corresponds to the case where the system is not detuned through the anticrossing. It indicates that it is possible to design complex pulses that can directly influence the competition between LZSM physics and charge noise. However, this is conditional on the dephasing time scale associated with charge noise. We notice that if $\gamma_2 = 10^9$ s $^{-1}$, then it is impossible to identify any coherent behavior [green and red traces, Fig. 9(e)].

Our results indicate that charge noise strongly affects the dynamics while spin relaxation only has a moderate effect. Although this behavior can be identified when comparing Fig. 9(a) with Figs. 9(b) and 9(c), it is best seen in Fig. 9(f) when comparing traces. An increase in the noise rate γ_2 leads to a substantial decrease of the oscillation visibility (blue and green traces). On the other hand, the visibility is only slightly diminished when relaxation is enhanced (blue and purple traces).

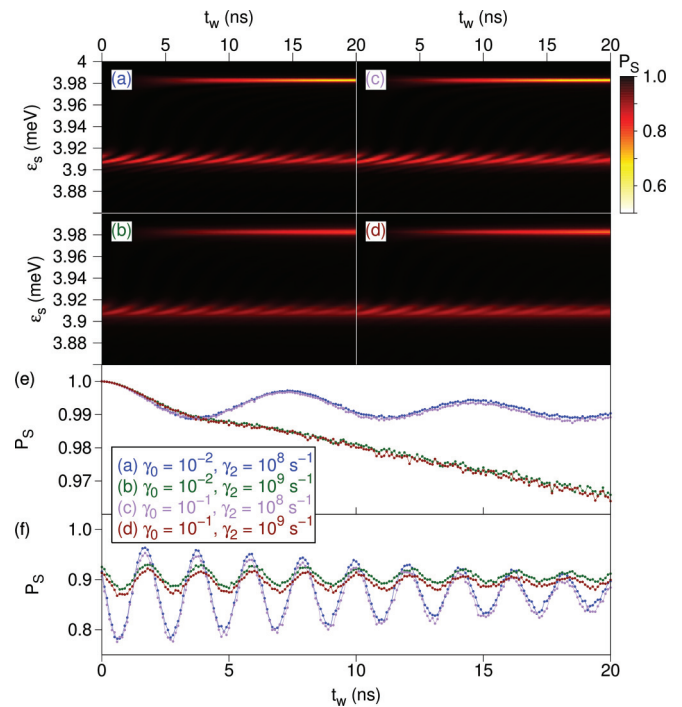


FIG. 9. (Color online) Singlet return probability P_S as a function of the waiting time t_w and final position ε_s obtained for a double-hat detuning pulse. Pulse details are given in the text. Here, we have set $B = 100$ mT, $u = 4$ meV, and $\tau = 5$ μeV for all plots. The parameters γ_0 and γ_2 are (a) $\gamma_0 = 10^{-2}$, $\gamma_2 = 10^8$ s $^{-1}$, (b) $\gamma_0 = 10^{-2}$, $\gamma_2 = 10^9$ s $^{-1}$, (c) $\gamma_0 = 10^{-1}$, $\gamma_2 = 10^8$ s $^{-1}$, and (d) $\gamma_0 = 10^{-1}$ s $^{-1}$, $\gamma_2 = 10^9$ s $^{-1}$. Figures (e) and (f) show cuts for case (a) in blue, (b) in dark green, (c) in purple, and (d) in dark red. The cuts are respectively taken before the anticrossing at $\varepsilon_s = 3.987$ meV and after at $\varepsilon_s = 3.908$ meV.

Here, charge noise has a drastic effect on spin dynamics. Since it leads to strong dephasing of the logical qubit states when spin and charge degrees of freedom are correlated, it results in a competition mechanism against LZSM interferometry.^{62–67} Since the hyperfine-mediated anticrossing is close to the charge anticrossing for reasonable values of B , charge noise also affects the dynamics during the passage through the anticrossing. As a result, the efficiency of the LZSM mechanism to create a coherent superposition or to produce coherent interferences is hindered, and thus the optimal state populations are not reached. This behavior can be identified in Fig. 9(f) when comparing traces obtained with the same relaxation rate, but different charge-noise rates (i.e., blue with green trace and purple with red trace). We clearly identify that the oscillation's visibility is smaller for larger values of γ_2 .

Energy relaxation processes have a weaker influence on spin dynamics than dephasing due to their dependence on the energy difference between the eigenstates of the system. These become important only when the system is held in close vicinity of the anticrossing, where relaxation is maximum [cf. Fig. 6(a)].

These results suggest that inhomogeneous dephasing due to nuclear spin fluctuations is not the only physical process that limits the coherence of a two-spin-based qubit, but also that

charge noise plays a major role. This is an important result for future devices made out of Si/SiGe which are reaching a maturity level comparable to GaAs.^{68–70} Silicon-based devices are very interesting candidates for spin-based quantum computing because the only stable isotope (²⁹Si) possessing a nuclear spin ($I = \frac{1}{2}$) has relatively low abundance $\approx 5\%$. Thus, hyperfine-induced decoherence is weaker than in GaAs-based nanostructures.⁶⁸

Consequently, we distinguish three time scales that govern the physics of partial spin adiabatic passage in DQDs. There is the rise time of the detuning pulse, the decoherence time T_2^* , and T_φ associated with charge-noise-induced dephasing. Ideally, we would like to have rise times shorter than T_φ to preserve any spin superposition state. But, this would render adiabatic transitions unlikely and therefore seriously hinder manipulation of the qubit. “Double-hat” pulses partially solve the problem, but for an even better result, it would be necessary to increase the coupling between the qubit states. In GaAs double quantum dots, it is possible to prepare a nuclear gradient field to enhance the hyperfine coupling,¹⁴ with the advantage of extending T_2^* . In almost nuclear spin free systems (Si- or C-based DQDs), it is possible to use micromagnets to artificially induce a coupling between the S-T₊ qubit states.⁷¹

V. CONCLUSIONS

We have developed a master-equation formalism to study the dynamics of a S-T₊ qubit in the vicinity of the hyperfine-mediated anticrossing. In comparison with previous theories that only included decoherence due to the hyperfine interaction with nuclear spins, we also include phonon-mediated hyperfine

spin relaxation and spin dephasing due to charge noise. We have also derived an effective two-level spin-charge Hamiltonian. In addition to previous theories, we take into account the charge degree of freedom. This property originates from the lowest-energy singlet state |S⟩ being a superposition of different charge configurations. Although the effective coupling between the S-T₊ qubit states is time dependent, its form still allows us to approximately reason in terms of LZSM physics.

With our formalism, we have compared results for different values of γ_0 and γ_2 . Our findings suggest that LZSM spin interferometry is largely inhibited by charge dynamics, and thus charge coherence has to be treated on equal footing with spin coherence. We have indeed demonstrated that the visibility of the coherent oscillations of a spin qubit is sensitive to the time scale associated with charge-induced spin dephasing. We have also shown that this interplay between charge and spin can prevent the observation of finite-time oscillations. Interestingly, this could lead to the development of an experimental protocol to measure the time scale associated with charge decoherence.

ACKNOWLEDGMENTS

The authors are grateful to H. Lu and A. C. Gossard for assistance with device fabrication. H.R. and G.B. acknowledge funding from the DFG within SPP 1285 and SFB 767. Research at Princeton was supported by the Sloan and Packard Foundations and the National Science Foundation through the Princeton Center for Complex Materials, DMR-0819860, and CAREER award, DMR-0846341.

*Current address: Department of Physics, University of Basel, Klingelbergstrasse 82, CH-4056 Basel, Switzerland.

¹D. Loss and D. P. DiVincenzo, *Phys. Rev. A* **57**, 120 (1998).

²R. Hanson, L. P. Kouwenhoven, J. R. Petta, S. Tarucha, and L. M. K. Vandersypen, *Rev. Mod. Phys.* **79**, 1217 (2007).

³K. Ono, D. G. Austing, Y. Tokura, and S. Tarucha, *Science* **297**, 1313 (2002).

⁴M. Elzerman, R. Hanson, L. H. Willems van Beveren, B. Witkamp, L. M. K. Vandersypen, and L. P. Kouwenhoven, *Nature (London)* **430**, 431 (2004).

⁵J. R. Petta, A. C. Johnson, J. M. Taylor, E. A. Laird, A. Yacoby, M. D. Lukin, C. M. Marcus, M. P. Hanson, and A. C. Gossard, *Science* **309**, 2180 (2005).

⁶F. H. L. Koppens, C. Buizert, K. J. Tielrooij, I. T. Vink, K. C. Nowack, T. Meunier, L. P. Kouwenhoven, and L. M. K. Vandersypen, *Nature (London)* **442**, 766 (2006).

⁷K. C. Nowack, F. H. L. Koppens, Yu. V. Nazarov, and L. M. K. Vandersypen, *Science* **318**, 1430 (2007).

⁸W. A. Coish and D. Loss, *Phys. Rev. B* **72**, 125337 (2005).

⁹J. M. Taylor, J. R. Petta, A. C. Johnson, A. Yacoby, C. M. Marcus, and M. D. Lukin, *Phys. Rev. B* **76**, 035315 (2007).

¹⁰S. Nadj-Perge, S. M. Frolov, E. P. A. M. Bakkers, and L. P. Kouwenhoven, *Nature (London)* **468**, 1084 (2010).

¹¹J. Levy, *Phys. Rev. Lett.* **89**, 147902 (2002).

¹²I. van Weperen, B. D. Armstrong, E. A. Laird, J. Medford, C. M. Marcus, M. P. Hanson, and A. C. Gossard, *Phys. Rev. Lett.* **107**, 030506 (2011).

¹³M. D. Shulman, O. E. Dial, S. P. Harvey, H. Bluhm, V. Umansky, and A. Yacoby, *Science* **336**, 202 (2012).

¹⁴S. Foletti, H. Bluhm, D. Mahalu, V. Umansky, and A. Yacoby, *Nat. Phys.* **5**, 903 (2009).

¹⁵A. V. Khaetskii, D. Loss, and L. Glazman, *Phys. Rev. Lett.* **88**, 186802 (2002).

¹⁶J. R. Petta, H. Lu, and A. C. Gossard, *Science* **327**, 669 (2010).

¹⁷H. Ribeiro, J. R. Petta, and G. Burkard, *Phys. Rev. B* **82**, 115445 (2010).

¹⁸H. Ribeiro, G. Burkard, J. R. Petta, H. Lu, and A. C. Gossard, *Phys. Rev. Lett.* **110**, 086804 (2013).

¹⁹L. D. Landau, *Phys. Z. Sowjetunion* **2**, 46 (1932).

²⁰C. Zener, *Proc. R. Soc. A* **137**, 696 (1932).

²¹E. C. G. Stückelberg, *Helv. Phys. Acta* **5**, 369 (1932).

²²E. Majorana, *Nuovo Cimento* **9**, 43 (1932).

²³S. N. Shevchenko, S. Ashhab, and F. Nori, *Phys. Rep.* **492**, 1 (2010).

²⁴W. D. Oliver, Y. Yu, J. C. Lee, K. K. Berggren, L. S. Levitov, and T. P. Orlando, *Science* **310**, 1653 (2005).

²⁵T. Calarco, A. Datta, P. Fedichev, E. Pazy, and P. Zoller, *Phys. Rev. A* **68**, 012310 (2003).

- ²⁶E. M. Gauger, S. C. Benjamin, A. Nazir, and B. W. Lovett, *Phys. Rev. B* **77**, 115322 (2008).
- ²⁷J. H. Cole, A. D. Greentree, L. C. L. Hollenberg, and S. Das Sarma, *Phys. Rev. B* **77**, 235418 (2008).
- ²⁸T. Hayashi, T. Fujisawa, H. D. Cheong, Y. H. Jeong, and Y. Hirayama, *Phys. Rev. Lett.* **91**, 226804 (2003).
- ²⁹J. R. Petta, A. C. Johnson, C. M. Marcus, M. P. Hanson, and A. C. Gossard, *Phys. Rev. Lett.* **93**, 186802 (2004).
- ³⁰I. I. Rabi, *Phys. Rev.* **51**, 652 (1937).
- ³¹R. Hanson and D. D. Awschalom, *Nature (London)* **453**, 1043 (2008).
- ³²A. Abragam, *Principles of Nuclear Magnetism* (Oxford University Press, New York, 1961).
- ³³N. Rosen and C. Zener, *Phys. Rev.* **40**, 502 (1932).
- ³⁴L. Allen and J. H. Eberly, *Optical Resonance and Two-Level Atoms* (Dover, New York, 1987).
- ³⁵F. T. Hioe, *Phys. Rev. A* **30**, 2100 (1984).
- ³⁶A. Bambini and P. R. Berman, *Phys. Rev. A* **23**, 2496 (1981).
- ³⁷Y. N. Demkov and M. Kunike, *Vestn. Leningr. Univ., Ser. Fiz. Khim.* **16**, 39 (1969).
- ³⁸F. T. Hioe and C. E. Carroll, *Phys. Rev. A* **32**, 1541 (1985).
- ³⁹J. Zakrzewski, *Phys. Rev. A* **32**, 3748 (1985).
- ⁴⁰Y. N. Demkov, *JETP* **45**, 195 (1963) [*Soviet. Phys. JETP* **18**, 138 (1964)].
- ⁴¹E. E. Nikitin, *Opt. Spektrosk.* **13**, 761 (1962) [*Opt. Spectrosc. USSR* **13**, 431 (1962)].
- ⁴²C. E. Carroll and F. T. Hioe, *J. Phys. A: Math. Gen.* **19**, 3579 (1986).
- ⁴³N. V. Vitanov and B. M. Garraway, *Phys. Rev. A* **53**, 4288 (1996).
- ⁴⁴M. Abramowitz and I. A. Stegun, *Handbook of Mathematical Functions* (Dover, New York, 1970), Chap. 6.
- ⁴⁵A. Erdélyi, W. Magnus, F. Oberhettinger, and F. G. Tricomi, *Higher Transcendental Functions*, Vol. II (McGraw-Hill, New York, 1953), Chap. 8.
- ⁴⁶H. Bluhm, S. Foletti, I. Neder, M. Rudner, D. Mahalu, V. Umansky, and A. Yacoby, *Nat. Phys.* **7**, 109 (2011).
- ⁴⁷S. A. Studenikin, G. C. Aers, G. Granger, L. Gaudreau, A. Kam, P. Zawadzki, Z. R. Wasilewski, and A. S. Sachrajda, *Phys. Rev. Lett.* **108**, 226802 (2012).
- ⁴⁸R. Hanson, L. M. K. Vandersypen, L. H. Willems van Beveren, J. M. Elzerman, I. T. Vink, and L. P. Kouwenhoven, *Phys. Rev. B* **70**, 241304(R) (2004).
- ⁴⁹G. Burkard, D. Loss, and D. P. DiVincenzo, *Phys. Rev. B* **59**, 2070 (1999).
- ⁵⁰Y. Kayanuma and S. Fukuchi, *J. Phys. B: At., Mol. Opt. Phys.* **18**, 4089 (1985).
- ⁵¹T. Usuki, *Phys. Rev. B* **56**, 13360 (1997).
- ⁵²J. Särkkä and A. Harju, *New J. Phys.* **13**, 043010 (2011).
- ⁵³H. Ribeiro and G. Burkard, *Phys. Rev. Lett.* **102**, 216802 (2009).
- ⁵⁴V. A. Abalmassov and F. Marquardt, *Phys. Rev. B* **70**, 075313 (2004).
- ⁵⁵X. Hu and S. Das Sarma, *Phys. Rev. Lett.* **96**, 100501 (2006).
- ⁵⁶G. Lindblad, *Commun. Math. Phys.* **48**, 119 (1976).
- ⁵⁷H. P. Breuer and F. Petruccione, *Theory of Open Quantum Systems* (Oxford University Press, Oxford, 2007).
- ⁵⁸A. V. Khaetskii and Y. V. Nazarov, *Phys. Rev. B* **64**, 125316 (2001).
- ⁵⁹A. G. Redfield, *IBM J. Res. Dev.* **1**, 19 (1957).
- ⁶⁰L. Chirrolli and G. Burkard, *Adv. Phys.* **57**, 225 (2008).
- ⁶¹L. DiCarlo, H. J. Lynch, A. C. Johnson, L. I. Childress, K. Crockett, C. M. Marcus, M. P. Hanson, and A. C. Gossard, *Phys. Rev. Lett.* **92**, 226801 (2004).
- ⁶²P. Ao and J. Rammer, *Phys. Rev. Lett.* **62**, 3004 (1989).
- ⁶³E. Shimshoni and Y. Gefen, *Ann. Phys. (NY)* **210**, 16 (1991).
- ⁶⁴M. Wubs, K. Saito, S. Kohler, P. Hänggi, and Y. Kayanuma, *Phys. Rev. Lett.* **97**, 200404 (2006).
- ⁶⁵K. Saito, M. Wubs, S. Kohler, Y. Kayanuma, and P. Hänggi, *Phys. Rev. B* **75**, 214308 (2007).
- ⁶⁶P. Nalbach and M. Thorwart, *Phys. Rev. Lett.* **103**, 220401 (2009).
- ⁶⁷P. P. Orth, A. Imambekov, and K. Le Hur, *Phys. Rev. A* **82**, 032118 (2010).
- ⁶⁸B. M. Maune, M. G. Borselli, B. Huang, T. D. Ladd, P. W. Deelman, K. S. Holabird, A. A. Kiselev, I. Alvarado-Rodriguez, R. S. Ross, A. E. Schmitz, M. Sokolich, C. A. Watson, M. F. Gyure, and A. T. Hunter, *Nature (London)* **481**, 344 (2012).
- ⁶⁹J. R. Prance, Z. Shi, C. B. Simmons, D. E. Savage, M. G. Lagally, L. R. Schreiber, L. M. K. Vandersypen, M. Friesen, R. Joynt, S. N. Coppersmith, and M. A. Eriksson, *Phys. Rev. Lett.* **108**, 046808 (2012).
- ⁷⁰K. Wang, C. Payette, Y. Dovzhenko, P. W. Deelman, and J. R. Petta, arXiv:1304.2640 [*Phys. Rev. Lett.* (to be published)].
- ⁷¹M. Pioro-Ladrière, T. Obata, Y. Tokura, Y.-S. Shin, T. Kubo, K. Yoshida, T. Taniyama, and S. Tarucha, *Nat. Phys.* **4**, 776 (2008).